

# Testing Galaxy Quenching Theories with Scatter in the Stellar to Halo Mass Relation

Jeremy L. Tinker<sup>1</sup>

<sup>1</sup>Center for Cosmology and Particle Physics, Department of Physics, New York University, New York, NY

8 March 2022

## ABSTRACT

We use the scatter in the stellar-to-halo mass relation to constrain galaxy evolution models. If the efficiency of converting accreted baryons into stars varies with time, halos of the same present-day mass but different formation histories will have different  $z = 0$  galaxy stellar mass. This is one of the sources of scatter in stellar mass at fixed halo mass,  $\sigma_{\log M_*}$ . For massive halos that undergo rapid quenching of star formation at  $z \sim 2$ , different mechanisms that trigger this quenching yield different values of  $\sigma_{\log M_*}$ . We use this framework to test various models in which quenching begins after a galaxy crosses a threshold in one of the following physical quantities: redshift, halo mass, stellar mass, and stellar-to-halo mass ratio. Our model is highly idealized, with other sources of scatter likely to arise as more physics is included. Thus, our test is whether a model can produce scatter lower than observational bounds, leaving room for other sources. Recent measurements find  $\sigma_{\log M_*} = 0.16$  dex for  $10^{11} M_\odot$  galaxies. Under the assumption that the threshold is constant with time, such a low value of  $\sigma_{\log M_*}$  rules out all of these models with the exception of quenching by a stellar mass threshold. Most physical quantities, such as metallicity, will increase scatter if they are uncorrelated with halo formation history. Thus, to decrease the scatter of a given model, galaxy properties would correlate tightly with formation history, creating testable predictions for their clustering. Understanding why  $\sigma_{\log M_*}$  is so small may be key to understanding the physics of galaxy formation.

**Key words:** galaxies:halos — galaxies: evolution

## 1 INTRODUCTION

In its simplest form, abundance matching connects galaxies with dark matter halos by the rank-order of both objects: the  $N$ th most massive galaxy resides in the  $N$ th most massive halo. The success of this paradigm rests on the assumption all halos of mass  $M_h$  have galaxies with mass stellar  $M_*$  inside them, regardless of the formation history of each halo. Any scatter in the relation is put in by-hand, post-facto. In essence, abundance matching rests on the idea that galaxy formation is a ‘path-independent’ process. Using the mean growth of halos, combined with measurements of the galaxy stellar mass function at various redshifts, one can use abundance matching to determine the average path of stellar mass growth in bins of halo mass (Conroy & Wechsler 2009; Behroozi et al. 2013a,b, hereafter B13, Moster et al. 2013). From this, one can show the efficiency of converting accreted baryons into stars,  $f_{\text{con}}$ . For massive halos—those with  $z = 0$  masses of  $10^{13} M_\odot$ , which will be the focus of this paper—this function monotonically increases with cosmic time up until it peaks at  $z \sim 2$ , whereupon it turns

over and galaxy growth quickly stalls. These results are in agreement with analyses of the stellar populations of massive galaxies, which imply rapid galaxy growth at high redshift with limited growth after  $z \sim 2$  (e.g., Thomas et al. 2005).

These results reflect the *average* formation history of galaxies within halos. However, dark matter halos of fixed mass can have widely varying formation histories. Two halos with a present-day mass of  $10^{13} M_\odot$  can differ by a factor of five at  $1-\sigma$  at  $z = 3$  (e.g., Wechsler et al. 2002). Any dependence of the baryonic conversion efficiency,  $f_{\text{con}}$ , with redshift—either explicitly, or implicitly through a dependence on  $M_h(z)$ ,  $M_*(z)$ , or other quantity—with break the path-independence of galaxy formation. Two halos with the same  $z = 0$  dark matter mass will *not* have the same mass galaxy in them. The distribution of halo formation histories is then one of the prime sources of scatter in the stellar mass to halo mass relation.

In this paper we will use the measurements of the scatter in stellar mass at fixed halo mass,  $\sigma_{\log M_*}$ , to put constraints on how  $f_{\text{con}}$  can vary with time for massive galaxies of present-day stellar mass  $M_* \approx 10^{11} M_\odot$ . These galaxies

form in halos of  $M_h \approx 10^{13} M_\odot$  (B13, Moster et al. 2013). We focus on massive galaxies for two reasons: first, these galaxies are nearly uniformly quiescent (Chen et al. 2012; Reid et al. 2016), thus the process that quenches star formation has already occurred in these halos. As we will show, because this process of quenching must occur over a short time span, it causes an extreme break of the path-independence of galaxy formation, and thus has a strong impact on  $\sigma_{\log M_*}$ . Second, although these galaxies are quite massive, abundance matching informs us that the buildup of stellar mass within these halos is due to in-situ star formation, and not by merging. B13 and Moster et al. (2013) both find that the fraction of stellar mass from in-situ growth in these halos is 90% at  $z = 0$  and 95% at  $z = 0.5$ , which is the redshift of the Baryon Oscillation Spectroscopic Survey (BOSS; Dawson et al. 2013) galaxy sample from which we will take observations of  $\sigma_{\log M_*}$ . Thus, the dominant source of scatter in stellar masses within these halos is star formation and not merging, which can dominate  $\sigma_{\log M_*}$  in higher mass halos (Gu et al. 2016).

Using the clustering and abundance of BOSS galaxies, Tinker et al. (2016) found  $\sigma_{\log M_*}$  for  $10^{13} M_\odot$  halos to be 0.16 dex. This value removes statistical errors from the stellar mass estimates, but does not remove systematic random errors incurred from the stellar mass estimation method itself. This value is in good agreement with other measurements of  $\sigma_{\log M_*}$  from other galaxy samples at lower redshifts (More et al. 2011; Reddick et al. 2013; Zu & Mandelbaum 2016). Although this is an upper limit, 0.16 dex is a shockingly low value for a quantity—stellar mass—that is influenced by a series of disparate processes, all with their own intrinsic distributions, such as metallicity, AGN feedback, supernovae feedback and winds, gas-rich merging, and the different baryonic accretion rates that different halos experience. The models we present in this paper are highly simplified, incorporating none of the physical effects just listed. Thus, our test for whether a model for quenching is valid is whether it can yield a value of  $\sigma_{\log M_*}$  below the observed value, leaving room for other sources of scatter from more physical effects.

Throughout this paper, we assume a flat- $\Lambda$ CDM cosmology with  $\Omega_m = 0.3$ ,  $\sigma_8 = 0.8$ , and  $h = 0.7$ . We will use redshift as our time unit quite often, especially in our model parameterizations, but will show plots as expansion factor  $a$ , which is a more natural time unit for the growth of galaxies.

## 2 MODELS

### 2.1 Parameterizing Star Formation Efficiency

We define the baryon conversion efficiency as

$$f_{\text{con}} \equiv SFR \times \left[ \frac{\Omega_b \dot{M}_h}{\Omega_m} \right]^{-1}, \quad (1)$$

where  $SFR$  is star formation rate,  $\Omega_b/\Omega_m$  is the universal baryon fraction (which we assume to be  $0.045/0.3 = 0.15$ ), and  $\dot{M}_h$  is the instantaneous growth rate of the halo. Inspection of the abundance matching results of B13 and Moster et al. (2013) shows that for low-mass halos, and in the absence of any external quenching mechanism,  $f_{\text{con}}$  can approximately be parameterized as a function that depends only on redshift:

$$f_{\text{con}}(z) = \begin{cases} f_0(M_{h0}) \left( \frac{1+z}{1+z_0} \right)^{\gamma_1} & \text{if } z > z_0 \\ f_0(M_{h0}) \left( \frac{1+z}{1+z_0} \right)^{\gamma_2} & \text{if } z \leq z_0 \end{cases} \quad (2)$$

where  $\gamma = -3$  at  $z > z_0$  and  $\gamma = 0$  and  $z \leq z_0$ ,  $f_0(M_{h0})$  is an overall amplitude that depends on  $z = 0$  halo mass, and  $z_0 = 1$ . The total stellar mass at any redshift  $z$  is

$$M_*(z) = \int_0^{t(z)} SFR(t) dt = \int_\infty^z f_{\text{con}}(z') f_b \dot{M}_h \frac{dt}{dz'} dz'. \quad (3)$$

To calculate the stellar mass growth for an individual halo, we use numerical halo merger trees (described in the next subsection). The trees calculate the mass of the halo at discrete time intervals, thus rather than implement equation (3) directly we use discrete summation over the timesteps, assuming that the integrand is a constant in time over each interval.

$$M_*(z_i) = \sum_i f_{\text{con}}(z_i) f_b \Delta M_{h,i}. \quad (4)$$

### 2.2 Parameterizing Star Formation Quenching

We parameterize the quenching of star formation by the quantity  $f_Q$ , such that  $SFR(z) \propto f_{\text{con}}(z) \times f_Q(z)$ . Figure 1 shows the time evolution of  $M_*(z)$  in present-day  $10^{13} M_\odot$  halos, as derived by B13. From these results, it is clear that quenching in these halos must happen over a short timescale, as stellar mass growth at  $z < 1$  is almost negligible. Thus we parameterize  $f_Q$  as an exponential function with free parameters governing the onset of quenching and its rapidity. We consider 6 different models for parameterizing the time evolution of  $f_Q$ . The forms implemented are all listed in Table 1.

- *Redshift quenching*: quenching begins at  $z < z_{\text{crit}}$ . Redshift quenching is a fairly ad-hoc model, although one can conceive of redshift-dependent quantities that may impact star formation. The results of this model can be thought of as applying the  $f_{\text{con}}$  results of B13 (or Moster et al. 2013) and applying them to individual halos.

- *Halo quenching*: quenching begins when  $M_h(z) > M_h^{\text{crit}}$ . The idea of a critical halo mass beyond which galaxy formation is curtailed is driven by numerical simulations that demonstrate that gas accretion onto halos undergoes a rapid transition at  $\sim 10^{12} M_\odot$  (Kereš et al. 2005, 2009; Dekel & Birnboim 2006). Below  $M_h^{\text{crit}}$ , gas is accreted cold and is deposited directly onto the central galaxy. Above this threshold, gas is shock heated to high temperature and gas cooling is significantly attenuated. Interpreting this threshold as a threshold for quenching star formation leads to a natural explanation of galaxy bimodality (Cattaneo et al. 2006).

- *Galaxy quenching*: quenching begins at  $M_*(z) > M_*^{\text{crit}}$ . The bimodality of galaxies can be seen most clearly in their stellar mass (e.g., Kauffmann et al. 2003), with a clear break in their  $z = 0$  properties at  $M_* \approx 10^{10.3} M_\odot$ . Such a scenario could be induced by instabilities in disk galaxies that occur after the disk becomes too massive. In the semi-analytic model of Bower et al. (2006), disk instabilities are the primary feeding mechanism for the central black hole, and thus the source of galaxy quenching. This model is described as ‘secular evolution’ in the Hopkins et al. (2008).

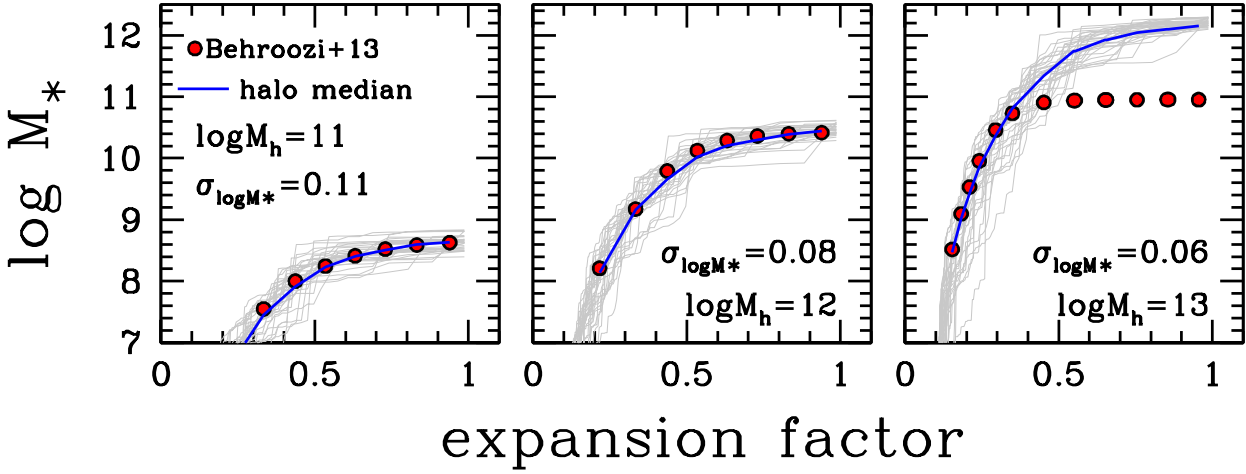


**Figure 1.** The stellar mass growth of halos of various masses. In each panel, the solid blue curve is the median value from a series of halo merger trees. This curve is fit to the results of Behroozi et al. (2013b), which are shown with the red circles. The evolutionary tracks of a subsample of halos are shown in the thin gray curves. For each halo, the same  $f_{\text{con}}(z)$  function is applied, thus the differences in stellar mass are all driven by the differences in halo mass growth. In each panel, the amplitude of  $f_{\text{con}}(z)$  is varied but the redshift-dependence is the same. This figure shows three things: (1) a single function of redshift can describe  $f_{\text{con}}$  for halos  $\leq 10^{12} M_{\odot}$ , as well as the high-redshift growth in massive halos (2) that  $10^{13} M_{\odot}$  halos undergo a rapid transition in their star formation efficiency at  $z \sim 2$ . This is a restatement of the previous results found in abundance matching studies and (3), different halo formation histories impart a scatter of  $\lesssim 0.1$  dex in  $\log M_*$  for a generic  $f_{\text{con}}(z)$  function.

- *Ratio quenching:* quenching begins when the ratio of the stellar mass to halo mass reaches a peak value,  $M_*/M_h = M_*/M_h^{\text{crit}}$ . This threshold was proposed by Leauthaud et al. (2012) to explain the apparent lack of evolution of peak value of  $M_*/M_h$  from  $z = 1 \rightarrow 0$ . The stellar to halo mass ratio is not monotonically rising, however, so the ratio itself is only used to determine the redshift of the onset of quenching, and we employ a secondary parameter to parameterize  $f_{\text{Q}}$ . Table 1 lists the three different implementations of  $M_*/M_h$ -quenching, where  $f_{\text{Q}}$  is parameterized by  $z$ ,  $M_h$ , and  $M_*$ . Where the critical value of each quantity is determined by the redshift at which  $M_*/M_h = M_*/M_h^{\text{crit}}$ .

Each model has four free parameters:  $f_0$ ,  $\sigma_{(x)}$ ,  $\alpha_{(x)}$ , and the critical threshold in parameter  $x$  that induces the quenching. The two remaining parameters in  $f_{\text{con}}$  are fixed to the best-fit values obtained from the lower-mass halos:  $z_0 = 1$  and  $\gamma = -3.0$ . We explore the posterior distributions of the free parameters using Markov Chain Monte Carlo (MCMC), using  $\chi^2$  of each model with respect to the B13 measurement of  $M_*(z)$  in  $10^{13} M_{\odot}$  halos to estimate the likelihood of each model. Due to asymmetries in some of the distributions of  $M_*(z)$  induced over the set of halo merger trees, we use the median value of  $M_*(z)$  rather than the mean, as well as the 68% range of values to estimate the scatter  $\sigma_{\log M_*}$ . The results of the MCMC chains are shown in Table 2. These will be discussed in the following section.

The models described above all assume that the quenching threshold, in each quantity, is a constant in time. There are two straightforward extensions of these models that we will discuss further in the draft.

- *Time-varying threshold:* Results of theoretical models of critical halo mass indicate that there is little, if any, variation

of the transitional mass scale between cold and hot accretion, but other effects may come into play, such as redshift evolution of metallicity. After presenting results of constant quenching thresholds in §3.2, we will incorporate a time-varying quenching barrier (for models that allow such freedom, which therefore excludes redshift quenching). We implement a straightforward linear dependence of the critical quantity on expansion factor  $X_{\text{crit}} = X_{\text{crit},0} + (a - 0.3) \times \beta$ . Where  $X$  represents  $M_h$ ,  $M_*$ , or  $M_*/M_h$ .

- *Stochastic quenching:* We allow the the critical threshold to vary in a stochastic manner from halo to halo using a random Gaussian deviate for halos  $i$ , i.e.,  $X_{\text{crit},i} = X_{\text{crit}} + G(\sigma_{\text{stoch}})$  where  $G$  is a Gaussian with zero mean and width  $\sigma_{\text{stoch}}$ . For halo and galaxy quenching  $X \equiv \log M_h^{\text{crit}}$  and  $X \equiv \log M_*^{\text{crit}}$ , and for redshift and ratio quenching,  $X$  is linear in  $z$  and  $M_*/M_h$ .

### 2.3 Halo Merger Trees

We use merger trees created by the publicly available code of Neustein & Dekel (2008). This algorithm is based off the extended Press-Schechter formalism but calibrated to match the results of numerical simulations. Although the code is able to create full trees for each final halo, the only quantity we are interested in is the time evolution of the mass of the main progenitor, for which the code is especially accurate.

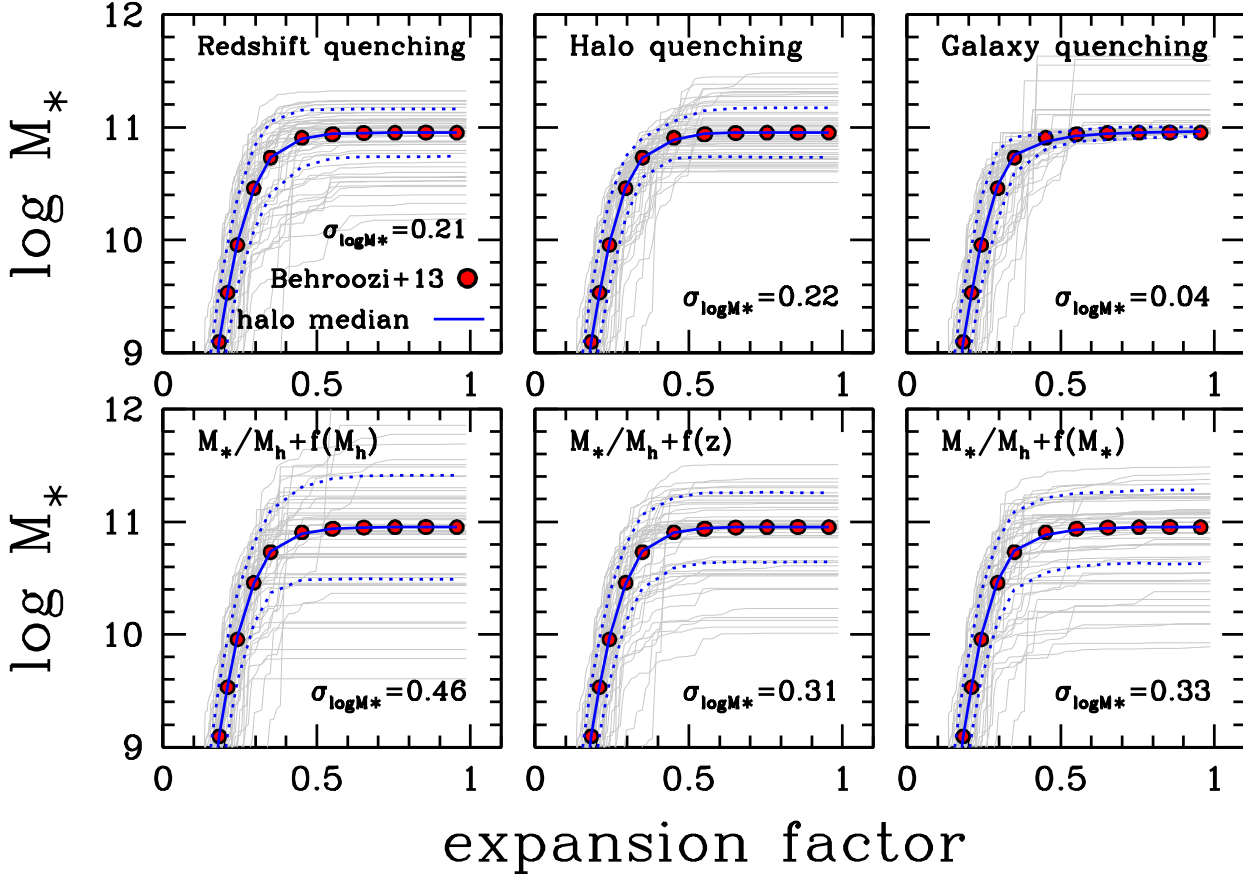


**Figure 2.** *Top Row:* Best fit models for redshift quenching, halo quenching, and galaxy quenching. The solid blue curves are the median of the set of halo merger trees, which are fit to the data of Behroozi et al. (2013b), shown with the red circles. A sample of individual halos are shown with the gray curves. The value of the scatter,  $\sigma_{\log M_*}$ , is shown for each model in the panel. The blue dotted curves show the 68% range of  $M_*$  around the median. *Bottom Row:* Same as the top row, but now for the three different models where the threshold for quenching is based on a critical  $M_*/M_h$  ratio, and after that point  $f_Q$  is parameterized by  $z$ ,  $M_h$ , and  $M_*$ , respectively.

Model	Form	Notes
Redshift Quenching	$f_Q(z) = \exp\left(\frac{z - z_{\text{crit}}}{\sigma_z}\right)^{\alpha_z}$	
Halo Quenching	$f_Q(M_h) = \exp\left(\frac{\log M_h^{\text{crit}} - \log M_h}{\sigma_h}\right)^{\alpha_h}$	
Galaxy Quenching	$f_Q(M_*) = \exp\left(\frac{\log M_*^{\text{crit}} - \log M_*}{\sigma_g}\right)^{\alpha_g}$	
Ratio Quenching + $f_Q(z)$	$f_Q(z) = \exp\left(\frac{z - z_{\text{crit}}}{\sigma_z}\right)^{\alpha_z}$	$z_{\text{crit}} = z(M_*/M_h = M_*/M_h^{\text{crit}})$
Ratio Quenching + $f_Q(M_h)$	$f_Q(M_h) = \exp\left(\frac{\log M_h^{\text{crit}} - \log M_h}{\sigma_h}\right)^{\alpha_h}$	$M_h^{\text{crit}} = M_h(z_{\text{crit}})$
Ratio Quenching + $f_Q(M_*)$	$f_Q(M_*) = \exp\left(\frac{\log M_*^{\text{crit}} - \log M_*}{\sigma_g}\right)^{\alpha_g}$	$M_*^{\text{crit}} = M_*(z_{\text{crit}})$

**Table 1.** Parameterization of the quenching function  $f_Q$ .

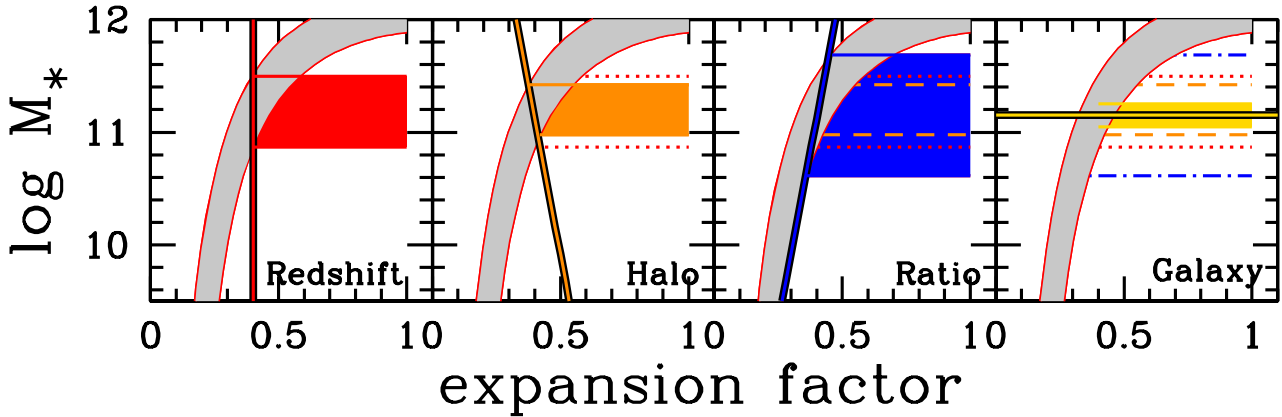


**Figure 3.** Pedagogical explanation for the different scatters induced by different quenching mechanisms. The gray shaded region in each panel represents the growth of galaxies in the absence of any quenching (c.f. Figure 1). Each physical property produces a threshold barrier with a different slope in the above diagram. The scatter is, to a reasonable approximation, the range on the  $y$ -axis where the barrier intersects the upper and lower bounds of the standard galaxy growth curves. Redshift scatter is thus a vertical barrier, and the scatter subsequent to quenching is the red shaded region. Halo quenching yields a barrier with a negative slope, shrinking the scatter.  $M_*/M_h$  quenching creates a threshold with steep positive slope, expanding the range of the post-quenching galaxy masses. Galaxy quenching simply stops growth at a constant horizontal barrier, yielding arbitrarily small scatter. More discussion on the slope of these barriers can be found in the text.

Model	$f_0$	$X_{\text{crit}}$	$\sigma(x)$	$\alpha(x)$
Redshift	$0.34 \pm 0.02$	$3.87 \pm 0.72$	$1.85 \pm 0.69$	$3.42 \pm 1.00$
Halo	$0.34 \pm 0.02$	$11.66 \pm 0.23$	$0.58 \pm 0.22$	$3.63 \pm 0.85$
Galaxy	$0.33 \pm 0.02$	$10.11 \pm 0.27$	$0.52 \pm 0.22$	$3.60 \pm 0.94$
Ratio+ $f(z)$	$0.34 \pm 0.02$	$0.019 \pm 0.006$	$1.26 \pm 0.47$	$3.03 \pm 1.08$
Ratio+ $f(M_h)$	$0.33 \pm 0.02$	$0.024 \pm 0.006$	$0.33 \pm 0.16$	$3.03 \pm 1.12$
Ratio+ $f(M_*)$	$0.33 \pm 0.02$	$0.027 \pm 0.006$	$0.37 \pm 0.19$	$3.36 \pm 1.02$
Redshift	0.34	3.14	1.10	2.14
Halo	0.33	11.40	0.84	4.81
Galaxy	0.33	9.91	0.73	4.95
Ratio+ $f(z)$	0.34	0.017	0.51	4.07
Ratio+ $f(M_h)$	0.34	0.014	1.71	3.36
Ratio+ $f(M_*)$	0.34	0.021	0.60	4.79

**Table 2.** Constraints on the quenching models. The top 6 lines show the mean and variance of each parameter in the model. The bottom 6 lines show the values of the best-fit model. Correlations between parameters and asymmetries in the posterior distributions of each parameter yield best-fit parameters that deviate from the mean values from the chains.

### 3 RESULTS

#### 3.1 Scatter in Intrinsic Physical Processes of Star Formation

Figure 1 shows the results of applying equation (4) to the numerical halo merger trees of various  $z = 0$  masses. These results do not include any quenching. At each halo mass, we fit for the amplitude of  $f_{\text{con}}$ ,  $f_0$ , by comparing the median of the simulated halos to the B13 data. For each halo mass considered, the best-fit value of  $f_0$  is 0.05, 0.27, and 1.40, respectively, going from low mass to high mass<sup>1</sup>. For  $M_h \leq 10^{12}$  a simple function for  $f_{\text{con}}$  fits the results for various

halo masses with only one tunable parameter. For massive halos, the results are quite different. As there is no quenching implemented in this figure, the models for  $10^{13} M_\odot$  halos are only fit to data at  $a < 0.3$  ( $z \gtrsim 2$ )<sup>2</sup>. The rapid attenuation of star formation at  $a \sim 0.3$  ( $z \sim 2$ ) is clear in these models. At  $a > 0.3$ , it is clear that the ‘universal’  $f_{\text{con}}$  function no longer applies to massive halos, and some form of process most occur to nearly extinguish the growth of the galaxies that form within them.

The thin gray lines show a subsample of the galaxy growth curves for individual halos. Although all halos in each panel are the same  $z = 0$  mass, the individual trajec-

<sup>1</sup> Note that  $f_0 > 1$  for these halos does *not* imply that they are converting more than 100% of their baryons into stars, as  $f_{\text{con}}$  goes as  $(1+z)^{-3}$  at the redshifts where this model is applied to massive halos.

<sup>2</sup> Fitting E.g. (4) to the data at all times leads to a best-fit model being a poor description of the data at all redshifts: the attenuation in stellar growth is too slow. The fit here is performed for pedagogical purposes only.

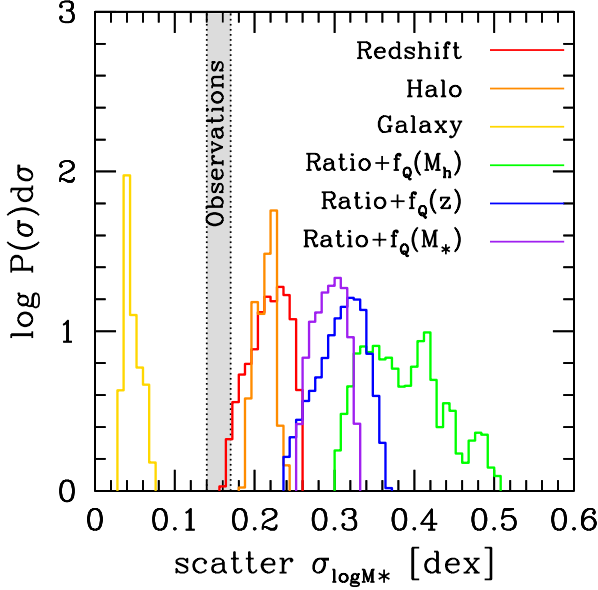


**Figure 4.** The posterior distributions of  $\sigma_{\log M_*}$  for each quenching model after being fit to the Behroozi et al. (2013b) stellar mass growth curves. The observations are taken from clustering measurements of BOSS galaxies in Tinker et al. (2016).

ries can differ substantially, especially at high redshift. Early forming halos accrete most of their mass (and thus most of their baryons) at redshifts when  $f_{\text{con}}$  is lower, thus they will have lower stellar masses at  $z = 0$  than late-forming halos. At late times ( $z < z_0$ ),  $f_{\text{con}}$  becomes independent of redshift, so any scatter in  $z = 0$  galaxy masses is fixed at that time. The values of  $\sigma_{\log M_*}$  monotonically decrease at halo mass increases. This is because larger halos grow at faster rates than smaller halos, thus their galaxies grow more from  $z = z_0 \rightarrow 0$ . The larger the fraction of stellar mass is created over this time frame, the more the scatter induced from growth during  $z > z_0$ .

The values of  $\sigma_{\log M_*}$  in Figure 1 are all comfortably below the observed value of 0.16 dex. However, the results of this figure put limits on all other sources of scatter (including, for example, having a non-universal  $f_{\text{con}}$  that varies from halo to halo in a systematic way that does not correlate with halo formation history).

### 3.2 Results with a Constant Quenching Threshold

Figure 2 shows the results of the best-fit parameter sets from the all models in 1. The panels show  $M_*(z)$  for the median of all halos, as well as a subsample of individual halos. In each panel, the scatter induced in each model is also listed; both redshift and halo quenching induce a scatter larger than the observed value of  $\sigma_{\log M_*} = 0.16$ . Galaxy quenching, unsurprisingly, creates a minimal scatter. For redshift quenching,  $f_Q(z)$  is the same for all halos. The product of  $f_{\text{con}}(z) \times f_Q(z)$  yields the mean baryonic conversion efficiency of  $10^{13} M_\odot$  halos found in B13 (c.f. their Figure 11). Halo quenching produces results very similar to redshift quenching, but the onset of quenching now varies from halo-to-halo. The similarity in the two models is due to the fact that  $\log M \propto -z$

(Wechsler et al. 2002), and so the mean  $f_Q(M_h)$  is very similar to  $f_Q(z)$ . The added variation in the time of quenching does not add to the  $z = 0$  variance in  $M_*$ , as we will discuss with Figure 3.

The bottom row of Figure 2 shows the results from the second three models in 1, where the quenching threshold is defined by  $M_*/M_h$ , but  $f_Q$  itself is parameterized by  $z$ ,  $M_h$ , and  $M_*$ . For these models,  $\sigma_{\log M_*}$  is significantly larger than the first three. The different behavior of all six models can be understood in the schematic outlines in Figure 3. The gray shaded region shows the  $\pm 1\sigma$  range of evolutionary tracks of galaxies within  $10^{13} M_\odot$  halos in the absence of any quenching (i.e., the right-hand panel of Figure 1). The thick colored lines indicate the ‘quenching barrier’ implied by each model in Table 1. Redshift quenching imposes a simple vertical barrier at fixed time. The range of post-quenching galaxy masses is indicated by the points on the  $y$ -axis where this barrier intersects the upper and lower bounds of the galaxy evolutionary tracks. For halo quenching, galaxies evolving on the  $+1\sigma$  track form in halos that grow rapidly at high redshift. Thus, these halos hit the threshold value of  $M_h$  at earlier times than those galaxies evolving on the  $-1\sigma$  track in slower-forming halos. Due to the tilted nature of the halo mass barrier, the range of galaxy mass is smaller than for redshift quenching. In detail, the value of  $\sigma_{\log M_*}$  does vary with the exact values of the free parameters in the models, thus it is possible to produce a redshift quenching model with smaller  $\sigma_{\log M_*}$  than a halo quenching model. However, as we will show in Figure 4, the median  $\sigma_{\log M_*}$  for halo quenching models is somewhat smaller than that for redshift quenching.

For ratio quenching, the trend of the barrier with redshift is opposite from halo quenching. At high redshift, halos grow faster than galaxies because  $f_{\text{con}} \propto (1+z)^{-3}$ . Thus, rapid-forming halos take longer to create enough stellar mass to meet the  $M_*/M_h^{\text{crit}}$  threshold. Halos that form later are accreting more of their mass at a time when  $f_{\text{con}}$  is higher and baryonic conversion is thus more efficient. Therefore these halos match  $M_*/M_h^{\text{crit}}$  earlier. The net effect is that the  $1\sigma$  range in post-quenching  $M_*$  is spread out significantly relative to the other models. The rightmost panel of Figure 3 shows galaxy quenching barrier as a horizontal line at fixed  $M_*$ . Thus, this model yields minimal scatter. The small scatter induced in the models is due to variations in halo growth over the period of time after quenching begins but before quenching is complete, or galaxies that grow significantly in the timestep in which they cross the barrier. In equation 4, quenching only begins on the timestep after the halo crosses the threshold. This is a choice in the implementation of the model, but would physically represent a scenario in which a halo crosses the threshold during a major starbursting event (such as a merger), and the quenching does not begin until after that burst of star formation declines.

Figure 4 shows the posterior distributions of  $\sigma_{\log M_*}$  for each model, marginalizing over the other parameters. The measurements of  $\sigma_{\log M_*}$  for  $10^{13} M_\odot$  halos from BOSS galaxies (Tinker et al. 2016) are shown with the gray shaded area. These measurements are at  $z \sim 0.5$ , but the dispersion in  $M_*$  in the models is essentially constant after quenching completes at  $z \sim 1$ . The features and asymmetries in the posterior distributions are real and not the result of noise or lack of convergence in the MCMC chains. The results here

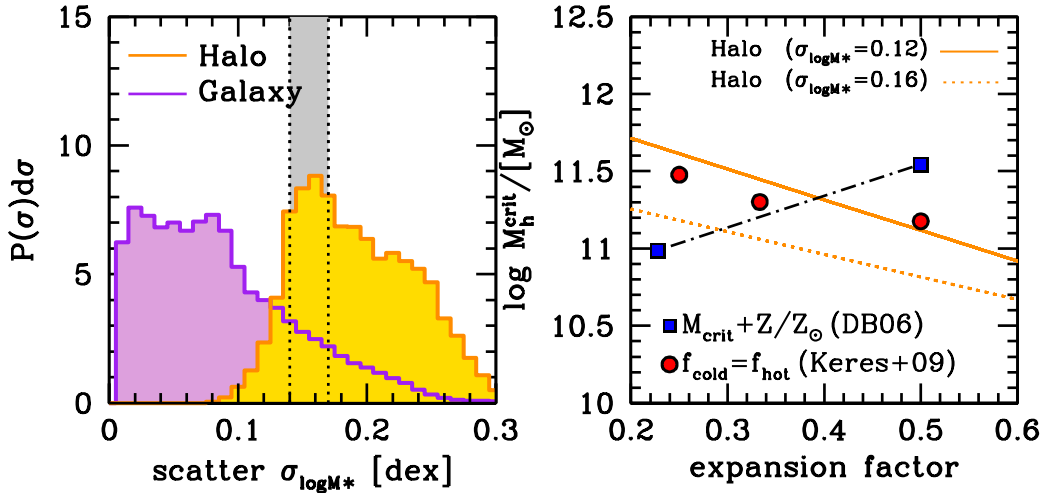


**Figure 5.** *Left panel:* The posterior distribution of  $\sigma_{\log M^*}$  for galaxy and halo quenching models in which the quenching threshold varies linearly with expansion factor. This freedom brings the halo quenching model into agreement with observational constraints on  $\sigma_{\log M^*}$ , yielding a 95% lower limit of 0.12 dex. The extra freedom also increases the scatter obtained in galaxy quenching, allowing value much higher than 0.16 dex. *Right Panel:* How the halo threshold changes with  $a$  in the various models. The two orange curves show the halo quenching threshold for  $\sigma_{\log M^*} = 0.16$  dex and for the lower limit of 0.12 dex. The red circles show the halo masses at which cold and hot gas accretion are equal in the simulations of Kereš et al. (2009). The blue squares connected by the dash-dot line show how  $M_h^{\text{crit}}$  would vary with time due to the increase in metallicity in massive galaxies over cosmic time (inferred from Dekel & Birnboim 2006; see text for further details and caveats.)

reflect those seen in the best-fit models of Figure 2; halo quenching and redshift quenching models yield results near  $\sigma_{\log M^*} \sim 0.22$ , while the different ratio quenching models yield values of  $\sigma_{\log M^*}$  that are much too high, ranging up to  $\gtrsim 0.5$  for ratio+ $f_Q(M_h)$ . Galaxy quenching yields  $\sigma_{\log M^*} \sim 0.04$ .

### 3.3 Increasing Freedom in the Models

As discussed in §2.2, models other than redshift quenching can be relaxed to allow the quenching threshold to vary in time. We have repeated the analysis for 5 of the 6 models that allow this freedom. The results for ratio quenching do not notably change, thus we will focus on halo and galaxy quenching from this point forward in this section.

The left panel in Figure 5 shows the posterior distribution of  $\sigma_{\log M^*}$  with this added freedom. The range of  $\sigma_{\log M^*}$  values is significantly expanded for both models, and both now overlap with the observed value. The right panel in Figure 5 shows examples of  $M_h^{\text{crit}}(z)$  that yield good fits to  $M_*(z)$  for two  $\sigma_{\log M^*}$  values. For halo quenching, models that reduce scatter have a tilted threshold such that  $M_h^{\text{crit}}$  decreases with time. In the constant- $M_h^{\text{crit}}$  model, late-forming halos will generally form galaxies above the mean. Tilting the threshold such that it is higher at higher redshift allows early-forming halos to convert a higher threshold of their baryons into stars before the onset of quenching, reducing the correlation between formation history and  $z = 0$   $M_*$ . As shown in the Figure, the slope of the barrier is independent of  $\sigma_{\log M^*}$  for values that are at and below the

observed value, but the amplitude increases as  $\sigma_{\log M^*}$  decreases. This enforces a lower limit on the value of  $\sigma_{\log M^*}$  achievable with halo quenching; quenching must be nearly complete by  $z \sim 1.5$ , when most halos at  $\sim 10^{12} M_\odot$ .

The theoretical expectation for how  $M_h^{\text{crit}}$  should vary—if at all—with redshift is not clear. Figure 5 shows results from two of the canonical studies. The filled circles show the transition halo mass scale between cold mode and hot mode accretion in the hydrodynamical cosmological simulations of Kereš et al. (2009), defined here as the halo mass scale where the fraction of gas being accreted in the hot and cold modes are equal. In this model, there is a slight decrease in  $M_h^{\text{crit}}$  with time that is in reasonable agreement with the data. However, one major simplification in these results is that there is no metal enrichment in the gas as the simulation evolves. Mannucci et al. (2009) find that the metallicity for massive galaxies increases by a factor of  $\gtrsim 5$  from  $z = 3$  to  $z = 0.7$  (parameterized as  $Z/Z_\odot$ . Dekel & Birnboim (2006), using one-dimensional hydro simulations, find a strong dependence of  $M_h^{\text{crit}}$  with metallicity. Combining these results with the observational measurements of  $Z/Z_\odot$ ,  $\log M_h^{\text{crit}}$  should increase by nearly half a decade over the timespan of active quenching, shown by the filled squares in the Figure. This calculation makes the assumption that gas metallicity only a function of time, independent of both the halo and galaxy formation history. Although this is likely to be an oversimplification in detail, the main point is that any increase of  $M_h^{\text{crit}}$  with time has the net effect of increasing  $\sigma_{\log M^*}$ , and  $Z/Z_\odot$  increases with time.

Scatter can be significantly increased in the galaxy

quenching model by a time-varying  $M_*^{\text{crit}}$ . Since a ‘horizontal’ quenching barrier produces no scatter, tilting this barrier in either direction will have the net effect of increasing this scatter.

### 3.4 Stochasticity in the Models

A more physical model may include some stochasticity in quenching—i.e., that the value of  $M_h^{\text{crit}}$  may vary randomly from halo to halo. To implement stochasticity, we choose a random Gaussian variable with zero mean and dispersion  $\sigma_{\text{stoch}}$ , which for the halo quenching model is in units of dex (i.e.,  $\log M_h^{\text{crit}}$ ). Stochasticity will only increase  $\sigma_{\log M_*}$ , but it is important to ask how much stochasticity is allowed by available data.

Figure 6 shows the range of models in the  $\sigma_{\log M_*}$ - $\sigma_{\text{stoch}}$  plane for the halo quenching model. In this analysis, we adopt of flat prior on  $\log \sigma_{\text{stoch}}$ . This model includes a time-varying quenching threshold. The lower envelope delineated by the chain indicates that, in order to be consistent with the data, any stochasticity in  $\log M_h^{\text{crit}}$  must be lower than 0.1 dex.

Calling once again on the dependence of  $M_h^{\text{crit}}$  on metallicity found in Dekel & Birnboim (2006), random variations of  $Z/Z_\odot$  between halos may induce such stochasticity in quenching. The scatter in  $Z/Z_\odot$  around  $10^{11} M_\odot$  galaxies is 0.2 dex (Gallazzi et al. 2005), which translates into a variation of 0.1 dex in  $\log M_h^{\text{crit}}$  (Dekel & Birnboim 2006, their Figure 4). Thus, if variations of  $Z/Z_\odot$  between galaxies of the same mass is random, this stochasticity would not allow any other contribution to  $\sigma_{\log M_*}$  and still be in agreement with the data. This is a strong assumption, but if metallicity is correlated with halo formation history it may be detectable through the effect of formation history on clustering.

## 4 SUMMARY AND DISCUSSION

We have implemented a simple model to explore how different models for quenching star formation in galaxies can impact the scatter of stellar mass at fixed halo mass,  $\sigma_{\log M_*}$ , for which we have excellent constraints from the clustering of massive galaxies. We test models in which quenching begins at some critical redshift,  $M_h$ ,  $M_*$ , or  $M_*/M_h$  ratio. We find:

- Under the assumption that the quenching threshold is constant with time, only galaxy quenching is consistent with the measurements of  $\sigma_{\log M_*}$ .
- The scatter imparted by halo and redshift quenching is somewhat larger than observations, while the scatter yielded by ratio quenching is nearly double that observed.
- To decrease the scatter induced by halo quenching,  $M_h^{\text{crit}}$  must decrease with time. This goes in the opposite direction implied by the growth of metallicity in galaxies.
- There is little to no room for any stochasticity in  $M_h^{\text{crit}}$  from halo-to-halo. The observed scatter in  $Z/Z_\odot$ , if uncorrelated with halo formation history, would raise  $\sigma_{\log M_*}$  above the observed values.
- Decreasing the scatter in each model would require strong correlations between galaxy properties, such as metallicity or mean stellar age, and halo formation history.

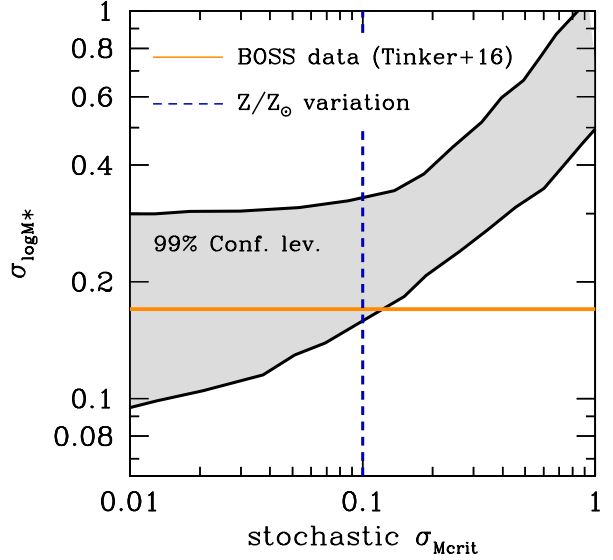


**Figure 6.** The effect on  $\sigma_{\log M_*}$  when including stochasticity in the halo quenching threshold. Stochasticity only has the effect of increasing the induced scatter. The shaded region shows the 99% confidence region for this model. The horizontal line indicates the measured value of  $\sigma_{\log M_*}$  from BOSS data. The dashed vertical line indicates the variation in  $\log M_h^{\text{crit}}$  induced by the scatter in metallicity, assuming that this scatter is uncorrelated with halo formation history.

Although galaxy quenching yields, by far, the lowest values of  $\sigma_{\log M_*}$ , there are some obvious questions that arise from this model. Observations of central galaxies within halos show that the quenched fraction varies smoothly with increasing galaxy mass, and not consistent with a threshold value (Weinmann et al. 2006). Stochasticity in the  $M_*^{\text{crit}}$  threshold may alleviate this tension, as well as some correlation of another galaxy property with the quenching threshold. Applying this model to the full galaxy population, rather than just massive galaxies, can resolve this question. This will be pursued in a future paper.

There are many simplifications and assumptions that are used to construct the models described above, but many—if not most—create testable predictions that may be constrained by existing data. The current spectroscopic sample of massive galaxies presently contains upwards of  $\sim 2$  million galaxies and reaches over 7 Gyr into the cosmic past through the combination of SDSS, BOSS, and now eBOSS data (for which the first clustering measurements have been published; Zhai et al. 2016). Although the quality of many of these spectra make detailed stellar population analysis untenable on a per-object basis, the clustering of these galaxies contains a wealth of information, well beyond the value of  $\sigma_{\log M_*}$  used here. At fixed  $M_*$ , the dependence of any galaxy property on halo formation history will show up in the clustering of those galaxies. This halo assembly bias has been shown conclusively in numerical simulations, and has recently been detected in cluster-sized dark matter halos observationally (Miyatake et al. 2016; More et al. 2016). Saito et al. (2016) used two-point clustering to demonstrate that  $z \sim 0.5$  BOSS galaxies are consistent with a model in

which the colors of massive galaxies are correlated with halo age.

For the fiducial implementations of galaxy and halo quenching, in which the threshold is constant in time, assembly bias is a natural consequence. Early-forming halos will have older stellar populations at fixed  $M_*$ , which could impart an assembly bias signal based on galaxy color, luminosity, and metallicity at fixed mass. Redshift and ratio quenching, on the other hand, yield little correlation between mean stellar age and the halo formation time. Different implementations of the halo quenching model yield different assembly bias signals as well. Halo quenching models with a time-varying threshold tend to reduce the amount of assembly bias in the models because they delay quenching in early-forming halo and accelerate it in late-forming halos. Further investigation, both through the clustering of massive galaxies and by using stellar population synthesis models to calculate the observable properties of galaxies with various mean stellar ages, will be fruitful in further differentiating models or constraining the parameter space of a specific model.

We have assumed that other physical mechanisms that effect star formation within dark matter halos would add to the scatter induced by variations in halo formation history. We have specifically focused on metallicity as a probable source of such scatter within the halo quenching model, either in the form of stochastic variations of the quenching threshold or a redshift dependence that would widen the scatter over the fiducial model. It is always possible that these physical mechanisms correlate with halo formation history in a way to reduce the scatter in stellar mass. For example, if metallicity correlated with halo formation history such that early-forming halos have higher metallicity than later-forming halos, the dependence of  $M_h^{\text{crit}}$  on  $Z/Z_\odot$  would help reduce scatter by allowing early-forming halos to convert more of their baryons into stars than they would in the constant threshold model. Such a model would create an assembly bias signal on the metallicity of massive galaxies.

Another assumption we have made in the construction of these models is that  $f_{\text{con}}$  is a universal function that only depends on  $z$ . Reducing the scatter in the pre-quenching phase of evolution would also reduce post-quenching scatter. Given the large variation in halo mass at  $z = 3$  for present day  $10^{13} M_\odot$  halos—roughly a factor of five—it is difficult to construct a model that creates minimal scatter in  $M_*$  within these halos at high redshift that isn't highly ad hoc. For  $z = 0$  halos below the quenching threshold, there still exists a scatter in stellar mass that is larger than that shown in Figure 1. A model in which  $f_{\text{con}}$  depends on  $z$  and some second parameter, such as  $M_h(z)$  or  $M_*(z)$ , may shrink the scatter at  $z \sim 2$ , but it is not clear that such a model would yield small scatter at  $z = 0$ , as well as reproduce the measurements of  $\text{SFR}(z)$  for galaxies of various masses, which is well fit by Equation (3) (B13, Moster et al. 2013).

Any strong conclusions made here depend on strong assumptions. However, this work represents a proof-of-concept that the scatter in the stellar to halo mass relation contains significant information for constraining the physics of galaxy formation. The simplified models presented here are sufficient to test simple models of galaxy formation and evolution, and as we isolate the region of parameter space that is consistent with observations, more sophistication can be

added to these models to properly explore this parameter space, and more data can be added by measuring clustering of massive galaxies to test for assembly bias in various physical quantities. Outside of empirical models of galaxy formation, semi-analytic and hydrodynamic explorations of galaxy formation physics should be utilizing  $\sigma_{\log M_*}$  in the assessment of their models. The processes that regulate star formation will also determine the scatter in the total amount of star formation. Understanding why  $\sigma_{\log M_*}$  is so small may be key to our understanding of how the present day galaxy population came to be.

## REFERENCES

- Behroozi P. S., Wechsler R. H., Conroy C., 2013a, ApJ, 762, L31  
 Behroozi P. S., Wechsler R. H., Conroy C., 2013b, ApJ, 770, 57  
 Bower R. G., Benson A. J., Malbon R., Helly J. C., Frenk C. S., Baugh C. M., Cole S., Lacey C. G., 2006, MNRAS, 370, 645  
 Cattaneo A., Dekel A., Devriendt J., Guiderdoni B., Blaizot J., 2006, MNRAS, 370, 1651  
 Chen Y.-M., Kauffmann G., Tremonti C. A., White S., Heckman T. M., Kovač K., Bundy K., Chisholm J., Maraston C., Schneider D. P., Bolton A. S., Weaver B. A., Brinkmann J., 2012, MNRAS, 421, 314  
 Conroy C., Wechsler R. H., 2009, ApJ, 696, 620  
 Dawson K. S., et al., 2013, AJ, 145, 10  
 Dekel A., Birnboim Y., 2006, MNRAS, 368, 2  
 Gallazzi A., Charlot S., Brinchmann J., White S. D. M., Tremonti C. A., 2005, MNRAS, 362, 41  
 Gu M., Conroy C., Behroozi P., 2016, ArXiv e-prints  
 Hopkins P. F., Cox T. J., Kereš D., Hernquist L., 2008, ApJS, 175, 390  
 Kauffmann G., Heckman T. M., White S. D. M., Charlot S., Tremonti C., Brinchmann J., Bruzual G., Peng E. W., Seibert M., Bernardi M., Blanton M., Brinkmann J., Castander F., Csábai I., Fukugita M., Ivezić Z., Munn J. A., Nichol R. C., Padmanabhan N., Thakar A. R., Weinberg D. H., York D., 2003, MNRAS, 341, 33  
 Kereš D., Katz N., Fardal M., Davé R., Weinberg D. H., 2009, MNRAS, 395, 160  
 Kereš D., Katz N., Weinberg D. H., Davé R., 2005, MNRAS, 363, 2  
 Kravtsov A., Vikhlinin A., Meshcheryakov A., 2014, ApJ, submitted, arXiv:1401.7329  
 Leauthaud A., Tinker J., Bundy K., Behroozi P. S., Massey R., Rhodes J., George M. R., Kneib J.-P., Benson A., Wechsler R. H., Busha M. T., Capak P., Cortés M., Ilbert O., Koekemoer A. M., Le Fèvre O., Lilly S., McCracken H. J., Salvato M., Schrabback T., Scoville N., Smith T., Taylor J. E., 2012, ApJ, 744, 159  
 Mannucci F., Cresci G., Maiolino R., Marconi A., Pastorini G., Pozzetti L., Gnerucci A., Risaliti G., Schneider R., Lehnert M., Salvati M., 2009, MNRAS, 398, 1915  
 Miyatake H., More S., Takada M., Spergel D. N., Mandelbaum R., Rykoff E. S., Rozo E., 2016, Physical Review Letters, 116, 041301  
 More S., Miyatake H., Takada M., Diemer B., Kravtsov A. V., Dalal N. K., More A., Murata R., Mandelbaum

- R., Rozo E., Rykoff E. S., Oguri M., Spergel D. N., 2016, ArXiv e-prints
- More S., van den Bosch F. C., Cacciato M., Skibba R., Mo H. J., Yang X., 2011, MNRAS, 410, 210
- Moster B. P., Naab T., White S. D. M., 2013, MNRAS, 428, 3121
- Neistein E., Dekel A., 2008, MNRAS, 383, 615
- Reddick R. M., Wechsler R. H., Tinker J. L., Behroozi P. S., 2013, ApJ, 771, 30
- Reid B., Ho S., Padmanabhan N., Percival W. J., Tinker J., Tojeiro R., White M., Eisenstein D. J., Maraston C., Ross A. J., Sánchez A. G., Schlegel D., Sheldon E., Strauss M. A., Thomas D., Wake D., Beutler F., Bizyaev D., Bolton A. S., Brownstein J. R., Chuang C.-H., Dawson K., Harding P., Kitaura F.-S., Leauthaud A., Masters K., McBride C. K., More S., Olmstead M. D., Oravetz D., Nuza S. E., Pan K., Parejko J., Pforr J., Prada F., Rodríguez-Torres S., Salazar-Albornoz S., Samushia L., Schneider D. P., Scóccola C. G., Simmons A., Vargas-Magana M., 2016, MNRAS, 455, 1553
- Saito S., Leauthaud A., Hearin A. P., Bundy K., Zentner A. R., Behroozi P. S., Reid B. A., Sinha M., Coupon J., Tinker J. L., White M., Schneider D. P., 2016, MNRAS
- Thomas D., Maraston C., Bender R., Mendes de Oliveira C., 2005, ApJ, 621, 673
- Tinker J., et al., 2016, submitted to ApJ, arXiv:1607.04678
- Wechsler R. H., Bullock J. S., Primack J. R., Kravtsov A. V., Dekel A., 2002, ApJ, 568, 52
- Weinmann S. M., van den Bosch F. C., Yang X., Mo H. J., 2006, MNRAS, 366, 2
- Zhai Z., et al., 2016, in preparation
- Zu Y., Mandelbaum R., 2016, MNRAS, 457, 4360